

Carleton College

Carleton Digital Commons

Faculty Work

Physics and Astronomy

2007

Kinetic Model for Sintering of Supported Metal Particles with Improved Size-Dependent Energetics and Applications to Au on TiO₂(110)

Stephen C. Parker
Carleton College

Charles T. Campbell
University of Washington

Follow this and additional works at: https://digitalcommons.carleton.edu/phys_faculty

 Part of the [Physics Commons](#)

Recommended Citation

Parker, Stephen C., and Charles T. Campbell., "Kinetic Model for Sintering of Supported Metal Particles with Improved Size-Dependent Energetics and Applications to Au on TiO₂(110)". *Physical Review B*, vol. 75, no. 035430, 2007. Available at: <https://doi.org/10.1103/PhysRevB.75.035430>. . [Online]. Accessed via Faculty Work. Physics and Astronomy. *Carleton Digital Commons*. https://digitalcommons.carleton.edu/phys_faculty/4

The definitive version is available at <https://doi.org/10.1103/PhysRevB.75.035430>

This Article is brought to you for free and open access by the Physics and Astronomy at Carleton Digital Commons. It has been accepted for inclusion in Faculty Work by an authorized administrator of Carleton Digital Commons. For more information, please contact digitalcommons.group@carleton.edu.

Kinetic model for sintering of supported metal particles with improved size-dependent energetics and applications to Au on TiO₂(110)

Stephen C. Parker¹ and Charles T. Campbell^{2,*}

¹*Department of Physics and Astronomy, Carleton College, Northfield, Minnesota 55057, USA*

²*Chemistry Department, University of Washington, Seattle, Washington 98195-1700, USA*

(Received 18 September 2006; published 31 January 2007)

A kinetic model for the sintering of metal particles on oxide or other support surfaces is derived and applied to simulate experimental measurements of the sintering of a model gold catalyst: gold nanoparticles supported on TiO₂(110). It follows the pioneering work of Wynblatt and Gjostein (WG), *Progress in Solid State Chemistry* (1975, p. 21), but removes several important assumptions that create dramatic errors in sintering rates for particles smaller than 6 nm in diameter, including (1) use of the Gibbs-Thomson relation assuming that the surface free energy of metal particles is independent of size, and (2) neglect of all but the first-order terms in a Taylor series expansion. Recent microcalorimetry measurements have shown these assumptions to be untrue in that metal particles smaller than 6 nm have much higher surface free energies than large particles. A modified bond-additivity model more accurately estimates particle energy versus size. This estimate was incorporated into the kinetic model of WG and applied to simulate the sintering of Au particles on TiO₂(110) as measured by temperature-programmed low-energy ion scattering. Our model reproduces well the broad temperature range over which sintering typically occurs in such experiments. This is analogous to accurate modeling of long-term sintering kinetics of metal nanoparticles under the isothermal conditions of real catalysis. These results also highlight problems with classical methods for determining the sintering mechanism based solely upon the shape of the sintered particle-size distribution.

DOI: [10.1103/PhysRevB.75.035430](https://doi.org/10.1103/PhysRevB.75.035430)

PACS number(s): 68.47.Jn, 68.43.Jk, 68.55.Ac, 68.60.Dv

I. INTRODUCTION

Oxide-supported metal nanoparticles are among some of the most important heterogeneous catalysts in use today. Among other functions, they are used for fuels conversion, pollution cleanup, chemicals production, and “green chemistry.” Many promising catalyst systems cannot be implemented industrially or are less efficiently utilized because sintering of the metal particles makes them inactive in the long term. That is, as with most late transition metal particles supported on oxides, these catalysts sinter or ripen with time, starting from a collection of many small, highly dispersed particles and eventually converting to their thermodynamically preferred state: fewer, larger particles.^{1–18}

Currently there is no reliable way of predicting the sintering behavior of any given metal-on-oxide catalyst, so any newly developed catalyst must be tested for the total duration of its required lifetime, often on the order of 1 yr. The time required for research and testing of a new catalyst could be cut dramatically if there were a method of accurately predicting long-term sintering based on short-term measurements. Thus, an accurate kinetic model for sintering is desirable.

In this paper, we present the derivation of such a kinetic model for sintering and demonstrate its accuracy by simulating kinetic measurements of the sintering of gold nanoparticles on TiO₂(110). We show that older models had been handicapped by an inaccurate picture of the particle-size dependence of the free energy of metal atoms in nanoparticles. Recent microcalorimetry experiments have made it possible to develop a better understanding of the change in particle energy with size and shown that a modified bond additivity (MBA) model more accurately reproduces the measured heat of adsorption, and thus the particle energies, for particles of

an fcc metal supported on MgO(100). We show how this model can be extended to other metals (and supports) and incorporated in a mechanistically accurate sintering kinetic model developed earlier by Wynblatt and Gjostein (referred to as “WG” below)¹ to markedly improve its accuracy.

Sintering of supported metal nanoparticle catalysts is generally thought to occur by one of two mechanisms:^{1–15} (1) Ostwald ripening or (2) particle diffusion/coalescence. In the Ostwald ripening mechanism, individual metal atoms (“monomers”) leave a metal particle and diffuse around on the support surface until they join another metal particle. Since the energy per atom is lower in larger particles, metal atoms stay longer in large particles. This ultimately leads to the growth of larger particles at the expense of smaller particles, which decrease in size and eventually disappear, since the smallest islands are slowly “two-dimensionally evaporated” away and added to the larger islands. The diffusing monomer may be in the form of a metal adatom on the oxide support, or as the metal’s carbonyl, oxide, chloride, or other complex adsorbed on the support.^{1,2,4,6,10} In the particle diffusion/coalescence mechanism, whole metal particles diffuse across the support surface until they come into contact with another particle and coalesce.

The kinetics of catalyst sintering and the elementary steps involved in sintering have been the subject of intensive research.^{1–4,6–10,12–36} Some of the best work in kinetic modeling of the sintering of supported metal particles is the work performed many years ago by Wynblatt and Gjostein (WG).^{1–3} It was used to explain extensive observations of Pt sintering on alumina. Their studies included kinetic models for both sintering mechanisms described above, with variations on both that could be applied when different elementary steps are rate determining. In general, these models de-

scribe with rate equations the rate of change of a metal particle's radius (R) with time. The WG models are attractive in that they include the details of metal atom migration and their energetics, which have been shown through many years of subsequent study to be essential for a complete understanding of sintering. Here we will focus mainly on their "interface-controlled" Ostwald ripening model, which is based on classical nucleation theory.¹ However, we also show that the improvement to that model developed here can be easily extended to their other models, where it is equally important.

Model catalysts consisting of gold nanoparticles supported on TiO₂(110) have been widely studied as a model of nanoparticle Au/TiO₂ catalysts, which are active in low-temperature CO oxidation and selective oxidation reactions.³⁷⁻⁴¹ Since there is a strong decrease in the Au-area-specific catalytic activity when the Au particles grow in size from 2–3 nm to 7–10 nm in diameter, sintering is a major problem for practical applications of such catalysts. As such, there have been many studies of the sintering kinetics and the kinetics of the elementary steps involved in sintering of Au nanoparticles on TiO₂(110), mainly by scanning tunnel microscopy (STM).^{12,21-25,29,30} It was concluded that sintering occurs mainly by the Ostwald ripening mechanism,^{12,21,22} although particle diffusion/coalescence also occurs, and may even dominate in some conditions.^{21,23-25}

Here, we also use temperature-programmed low-energy ion scattering (TP-LEIS) to monitor the sintering kinetics of a model catalyst consisting of gold nanoparticles supported on TiO₂(110). TP-LEIS is an extremely surface sensitive technique that directly measures the percentage of the oxide surface covered by metal nanoparticles as a function of temperature during a linear heating ramp.⁴² This technique provides a quantitative measurement of the sintering kinetics over a broad range of temperatures and dispersions in one fast experiment.⁴² The results are simulated here using the sintering kinetic model derived here, which much more accurately reproduces the measured sintering kinetics than earlier models, and does so using physically reasonable values for the few adjustable parameters. A preliminary report of some of these results has been presented elsewhere.⁴³

II. EXPERIMENTAL

Temperature-programmed low-energy ion scattering (TP-LEIS) experiments were performed in a Leybold-Heraeus ultrahigh vacuum chamber described elsewhere,⁴⁴ with a base pressure of $\sim 10^{-10}$ mbar. The methods for preparing the TiO₂(110) surface, vapor depositing Au on this surface, and measuring the Au surface coverage were described previously.⁴⁵

In standard He⁺ LEIS experiments, the sample surface is bombarded with He⁺ ions, while an ion energy analyzer scans through a range of energies of the scattered He⁺ ions. The He⁺ ion beam was generated with the LK Technologies ion gun, run at 2.0×10^{-8} mbar of He with a 1250 eV beam energy, which gave a He⁺ ion flux of $\sim 0.2 \mu\text{A}/\text{cm}^2$. The LEIS spectra were measured with a hemispherical energy analyzer at a scattering angle of 125°. Peaks appear in the

resulting ion-intensity spectrum for any elements in the surface, with elements at higher masses appearing at higher energies. He⁺ LEIS is an extremely surface sensitive technique: scattered He⁺ ions have a high probability of neutralization, and this probability approaches unity for ions that penetrate more than ~ 0.1 nm into the electron cloud of the topmost atomic layer before elastic scattering.^{45,46} This results in a LEIS spectrum with peaks only for the elements in the topmost atomic layer of the surface. Dividing the Au LEIS peak area for Au particles on TiO₂ by that for a thick, continuous, clean Au film provides a ratio equal to the percentage of oxide surface covered by the Au particles.⁴⁵

In the TP-LEIS experiments below, the analyzer was set to repetitively monitor intensity at one energy (here, the LEIS peak energy for Au) with a 1.0 s sampling time, while the sample temperature was ramped at 1 K/s. Thus, TP-LEIS tracks in real time the fraction of the TiO₂ surface covered by gold particles, thus providing a direct kinetic measure of their sintering. As temperature increases, the Au particles sinter into thicker and larger particles that cover less of the surface, observed as a decrease in the Au LEIS signal with temperature (monitored once every degree K or every second). The instrumentation and methods for TP-LEIS have been described in detail elsewhere.⁴²

III. DERIVATION OF SINTERING KINETIC EQUATIONS

Wynblatt and Gjostein (WG) derived kinetic equations for sintering that describe the time evolution of island radii from some initial size distribution.¹ We focus in this section only on their equations which were derived assuming that sintering is dominated by the Ostwald ripening mechanism, whereby metal monomers detach preferentially from small metal islands, diffuse randomly across the oxide substrate, and attach preferentially to larger metal islands. Here, we will refer to these diffusing monomers as metal "atoms" or "adatoms," but the same equations apply if they are metal-ligand complexes of the types mentioned above. These monomers are assumed to have sites on the surface of both the metal particles and the oxide substrate. These WG equations were derived in two different rate-limiting regimes: the ripening can be rate limited either by a detachment/attachment process of metal atoms at the edge of the island ("interface control") or by the diffusion of metal adatoms from one island to another ("diffusion control"). Each metal island is assumed to be a spherical segment with an equilibrium shape defined by the metal/oxide contact angle, θ (Fig. 1). The spherical radius of the island is given by R , whereas the actual radius of the island's interface with the oxide substrate's surface is given by $R \sin \theta$ (Fig. 1). They derived that the radius of each particle of interest varies in time (t) in the interface-control limit as:

$$\frac{dR}{dt} = \frac{\sin(\theta) a \beta' \beta c_p^{\text{eq}} \gamma_m \Omega^2}{\alpha_1 k T R^2} \left(\frac{R}{R^*} - 1 \right), \quad (1)$$

while in the diffusion-control limit, it varies as

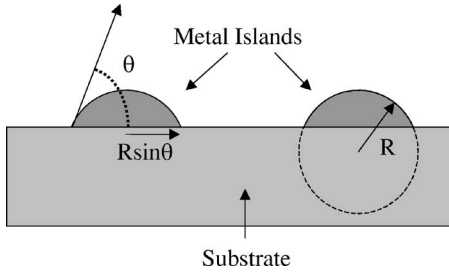


FIG. 1. A schematic representation of the model used here for a metal island on a substrate surface as a segment of a sphere (of radius R). The radius of the circular island/substrate interface is $R \sin(\theta)$, where θ is the contact angle of the metal island with the substrate.

$$\frac{dR}{dt} = \frac{D_1 \beta c_p^{\text{eq}} \gamma_m \Omega^2}{\ln[L/R \sin(\theta)] \alpha_1 k T R^3} \left(\frac{R}{R^*} - 1 \right). \quad (2)$$

In Eqs. (1) and (2), a is the interatomic spacing, c_p^{eq} is the equilibrium monomer concentration on an infinitely large metal particle, γ_m is the metal surface energy (assumed to be independent of radius), Ω is the atomic volume of the bulk metal (i.e., the molar volume of the bulk metal, easily calculated from its molar mass divided by its bulk, solid density and Avogadro's number), k is Boltzmann's constant, T is the temperature (in K), R is the radius of the island, α_1 is a geometrical factor related to the island structure equal to $(2 - 3 \cos \theta + \cos^3 \theta)/4$ (see Fig. 1), L is the distance (from the island center) required for the monomer concentration on the oxide substrate to reach its far-field limit of \bar{c}_s (see Fig. 2), D_1 is the monomer diffusivity across the substrate, $\beta' = \nu_s \exp[-H_m^s/kT]$ (where ν_s is the vibrational frequency of a monomer in a substrate site and H_m^s is its diffusion barrier on the substrate, Fig. 2), and $\beta = \nu_p / \nu_s \exp[-H_{ps}/kT]$ (where ν_p is the vibrational frequency of a monomer on a particle and H_{ps} is the energy difference between a monomer on the substrate and a monomer on the particle, Fig. 2). The term R^* is defined as the inverse of the surface average of the inverse island radii, or $R^* = 1/\langle 1/R \rangle$. Note that dR/dt depends on the value of R , and that its sign is negative when the ratio R/R^* is less than unity. Thus R^* is also the critical value of R below which particles get smaller with time, and above which they get larger.

In the following, we outline the steps that lead to these WG equations, but also derive slightly different equations that remove some of the inherent assumptions that we will prove were not justified. This leads to more accurate formulas for modeling and predicting sintering kinetics.

First, WG (Ref. 1) consider a particle that has the shape of a spherical segment, as shown in Fig. 1. The volume of such a particle is given by $V = 4/3 \pi R^3 \alpha_1$ and the surface area of the particle is given by $4 \pi R^2 \alpha_2$, where $\alpha_2 = (1 - \cos \theta)/2$. They assumed that the particle-size probability distribution, $f(R, t)$, is continuous and that the total volume of the islands remains constant (since there is no incoming flux or desorption that will be adding metal into or subtracting metal from the system). These two constraints on the system require that

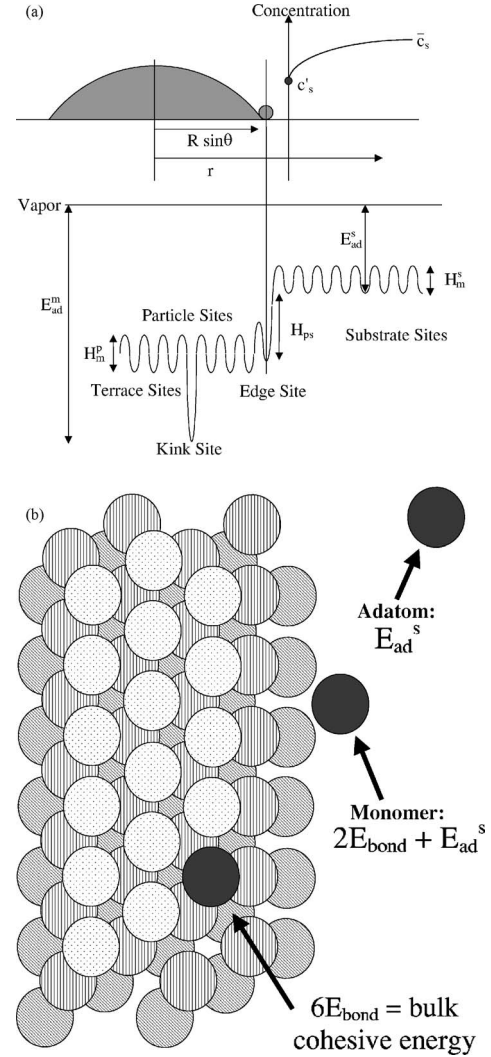


FIG. 2. (a) A schematic representation of the concentration of adatoms on the substrate surface as well as the energetics on the both the substrate and the particle (from Ref. 1). The gray sphere refers to a monomer on the particle, i.e., a metal atom bonded to the edge of a particle, which is the key intermediate in transport of metal atoms between metal particles and the support surface. For an infinite-size particle, E_{ad}^m is just the metal's bulk sublimation energy (ΔH_{sub}), since sublimation is simply desorption from kink sites on the bulk metal surface. (b) A top-down view of a metal island, an atom on its edge (i.e., a "monomer on a particle," shaded), and an adatom on the substrate (also shaded). Within a pairwise bond-additivity model where the average bond energy between two metal atoms is E_{bond} , $H_{\text{ps}} = 2E_{\text{bond}}$, and the difference in energy between metal atoms in huge particles (i.e., the metal's bulk cohesive energy) and a monomer on a particle equals $4E_{\text{bond}} - E_{\text{ad}}^s$, where E_{ad}^s is the adsorption energy of a metal atom on the oxide substrate.

$$\frac{\partial f}{\partial t} = - \frac{\partial}{\partial R} \left(f \frac{dR}{dt} \right) \quad (3)$$

and

$$\frac{4}{3} \pi \alpha_1 \int_0^{\infty} f R^3 dR = \text{constant}. \quad (4)$$

Two different rates will be important in this derivation: the net rate at which adatoms (monomers) leave the substrate to add to the particle of interest (J_p) and the net rate of diffusion of adatoms toward the particle of interest (J_s). The perimeter, P , of a metal island with a spherical radius of R as shown above is given by $P=2\pi R \sin \theta$. A concentration gradient of adatoms exists on the surface of the nearby substrate surface as a result of energy wells at the edges of islands. These wells exist due to the stronger bonding of atoms at the edge of the island compared to that on the substrate surface. When atoms reach these lower energy states, they become trapped at these sites for a much longer time than on the rest of the surface. The concentration of adatoms on the substrate sites immediately adjacent to the particle will be denoted by c'_s , and the average concentration of adatoms far from the cluster (i.e., in the far-field limit) will be denoted by \bar{c}_s (see Fig. 2).

For a metal atom to leave a particle and go onto the substrate surface (or vice versa), it passes through a transient intermediate state referred to by WG as a “monomer on the particle,” shown as the gray sphere in Fig. 2. Following WG, we take the definition of this monomer on the particle to be a metal atom on the edge of the particle that only has two nearest-neighbor bonds to other metal atoms in the particle but is also bonded to the support (substrate). Neglecting all but nearest-neighbor interactions, the energy of this intermediate is independent of particle size. The strict definition of the structure of this species is not important, provided that one is consistent in calculating (and considering) its energetics throughout the derivation, since its exact energy will not appear in the final rate equations below. The concentration of monomers on the particle will be denoted by c_p .

The net rate of adatom addition onto the particle of interest can be found by taking the difference between the number of adatoms moving onto the particle and the number of adatoms moving off the particle. The activation barrier for an adatom to move from a site on the oxide substrate onto a particle’s edge (i.e., to become a “monomer on the particle”) is assumed to be equal to the diffusion barrier of a metal adatom on the substrate, H_m^s (Fig. 2). The energetic difference between a monomer on the particle (i.e., at an edge site) and an adatom on the substrate is given by H_{ps} (uphill in energy to detach from the particle), so therefore the activation barrier for the monomer to break free from the particle and move onto to the substrate will be just $H_{ps}+H_m^s$ (Fig. 2). The rate for an elementary process can be found from the concentration of the reactant state, the energetic barrier it must overcome, and the number of sites into which the transition can take place. Therefore, the rate onto the particle is given by $c'_s a P \beta'$, which is just the product of the total number of adatoms on the oxide surface sites immediately adjacent to the sites for binding onto the edge of an island of perimeter length P ($c'_s a P$) and the rate constant β' . In a similar fashion, the rate leaving the particle is given by $c_p P a \beta \beta'$. Taking the difference between these two contributions gives us that the net rate onto the particle J_p is

$$J_p = 2\pi R \sin(\theta) a \beta' (c'_s - c_p \beta) = X(c'_s - c_p \beta), \quad (5)$$

where $X=2\pi R \sin(\theta) a \beta'$.

The second important rate, the net rate at which adatoms on the substrate diffuse toward a particle, can be found by examining the concentration gradient near an island. Using Fick’s Law of diffusion, one can say that the rate toward the particle through a circle around it at radius r is given by $J_s = 2\pi r D_1 (dc/dr)$. By separating out the relevant variables to each side of this equation, we have: $(J_s/2\pi r) dr = D_1 dc$. Integrating (with the radii limits of R to L and with the respective concentration limits of c'_s and \bar{c}_s), and solving for J_s gives

$$J_s = \frac{2\pi D_1}{\ln[L/R \sin(\theta)]} (\bar{c}_s - c'_s) = Y(\bar{c}_s - c'_s), \quad (6)$$

where

$$Y = \frac{2\pi D_1}{\ln[L/R \sin(\theta)]}.$$

If we assume that the adatom concentration immediately adjacent to a particle quickly establishes a steady state value, $dc'_s/dt \approx 0$, then we can set $J_p = J_s$ and solve for c'_s . It can then be substituted into Eq. (5) to give

$$J_p = \frac{XY}{X+Y} (\bar{c}_s - c_p \beta). \quad (7)$$

The concentrations \bar{c}_s and c_p can be expressed in terms of the concentration of monomers on the support in equilibrium with infinite size particle (c_s^{eq}), and the concentration of monomers on a particle (i.e., the key intermediates at particle edge sites) at equilibrium for an infinite size particle (c_p^{eq}). From Fig. 2, we see that the energy difference between a monomer on the support and metal atom at a kink site on an infinite particle is $\Delta H_{sub} - E_{ad}^s$, and that the energy difference between a monomer on the support and metal atom at a kink site on an infinite particle is $\Delta H_{sub} - E_{ad}^s - H_{ps}$, where ΔH_{sub} is the bulk metal’s sublimation energy (i.e., the metal atom’s adsorption energy on a metal particle, E_{ad}^m , for an infinite-size particle) and E_{ad}^s is the adsorption energy of a metal adatom on the support. Neglecting the small vibrational entropy differences between these species, c_s^{eq} equals $\exp[-(\Delta H_{sub} - E_{ad}^s)/kT]/a^2$, and c_p^{eq} equals $\exp[-(\Delta H_{sub} - E_{ad}^s - H_{ps})/kT]/a^2$. (This can be proven by equating adsorption/desorption rates into the gas phase for atoms in the surface of a bulk metal solid and comparing to the expression for those rates for a monomer on a particle, assuming unit sticking probability in both cases.)

Following WG, we will assume that the chemical potential (μ) of the metal atoms in a metal particle with a radius of curvature of R is different from that in a metal particle of infinite radius (i.e., bulklike) in the same way it would for an atomic liquid, and so is given by

$$\mu(R) - \mu(\infty) = \frac{2\gamma_m \Omega}{R}, \quad (8)$$

where γ_m is the surface free energy of the metal.^{2,3} This is called the “Gibbs-Thomson relation” by WG.² Remember that the chemical potential of diffusing adatoms or monomers in equilibrium with a particle of radius of curvature R must equal $\mu(R)$, but also must vary as $kT \ln(\text{concentration})$.

Combined with Eq. (8), this gives a relationship for the concentration of adatoms on the substrate in equilibrium with a particle of radius R^* ,

$$\bar{c}_s = c_s^{\text{eq}} \exp\left[\frac{2\gamma_m\Omega}{kTR^*}\right] = c_s^{\text{eq}} \left[1 + \frac{2\gamma_m\Omega}{kTR^*} + \dots\right], \quad (9)$$

and a similar expression for the concentration of monomers on a particle of radius R ,

$$c_p = c_p^{\text{eq}} \exp\left[\frac{2\gamma_m\Omega}{kTR}\right] = c_p^{\text{eq}} \left[1 + \frac{2\gamma_m\Omega}{kTR} + \dots\right], \quad (10)$$

where in each case a Taylor series expansion is used. These equations are analogous to the Kelvin equation for the radius dependence of the equilibrium vapor pressure above a liquid droplet.⁴⁷

WG used only the first two terms in the Taylor expansions of Eqs. (9) and (10), but that assumption is incorrect for very small particles, since the exponential term is not $\ll 1$ when the particle diameter is less than 10 nm. For instance, in the example of Pb that we show later, the exponent is ~ 10 for a 2 nm diameter Pb island at 300 K. We will not use the Taylor expansion of these terms and will derive alternative equations using instead the full exponentials in our treatment.

Substituting the expressions in the left sides of Eqs. (9) and (10) into Eq. (7), gives

$$J_p = \frac{XY}{X+Y} \left(c_s^{\text{eq}} \exp\left[\frac{2\gamma_m\Omega}{kTR^*}\right] - \beta c_p^{\text{eq}} \exp\left[\frac{2\gamma_m\Omega}{kTR}\right] \right). \quad (11)$$

When recognizing that $c_s^{\text{eq}} = \beta c_p^{\text{eq}}$ (note that β is just the equilibrium constant for the interconversion between adatoms on the substrate and monomers on the particle), Eq. (11) can be reduced to

$$J_p = \frac{XY}{X+Y} \beta c_p^{\text{eq}} \left(\exp\left[\frac{2\gamma_m\Omega}{kTR^*}\right] - \exp\left[\frac{2\gamma_m\Omega}{kTR}\right] \right). \quad (12)$$

At this point, it becomes useful to examine the two different rate-limiting regimes. When $X \gg Y$, the rate will be limited by diffusion, whereas when $Y \gg X$, it will be limited by the interface. In the interface control limit, J_p reduces to

$$J_p = Y \beta c_p^{\text{eq}} \left(\exp\left[\frac{2\gamma_m\Omega}{kTR^*}\right] - \exp\left[\frac{2\gamma_m\Omega}{kTR}\right] \right), \quad (13)$$

while the diffusion limit reduces to

$$J_p = X \beta c_p^{\text{eq}} \left(\exp\left[\frac{2\gamma_m\Omega}{kTR^*}\right] - \exp\left[\frac{2\gamma_m\Omega}{kTR}\right] \right). \quad (14)$$

Since we will be using the interface-control limit in the simulations outlined later in this paper, we will discuss only this limit in the rest of this section. The same analysis could be carried out for the diffusion limit, but it is not shown. One of the constraints mentioned in the beginning of this derivation was that the total volume of the islands was conserved (i.e., no metal desorption or impingement onto the surface). Depending on the size of a given island, each individual island will either grow or shrink. The amount by which the volume of a particle (V) will change is proportional to the net rate to the particle, J_p . We can write down the time rate of

change of volume of an island of radius R as

$$\frac{dV}{dt} = \frac{d}{dt} \left(\frac{4}{3} \pi R^3 \alpha_1 \right) = 4 \pi R^2 \alpha_1 \left(\frac{dR}{dt} \right) = J_p \Omega. \quad (15)$$

Upon substituting J_p into this equation and solving for dR/dt , the interface-controlled time rate of change of island radius is

$$\frac{dR}{dt} = \frac{\sin(\theta) a \beta' \beta c_p^{\text{eq}} \Omega}{2\alpha_1 R} \left(\exp\left[\frac{2\gamma_m\Omega}{kTR^*}\right] - \exp\left[\frac{2\gamma_m\Omega}{kTR}\right] \right). \quad (16a)$$

It is this equation that we will be using below when examining what we will call the ‘‘Gibbs-Thomson model’’ or ‘‘GT model.’’ We therefore rewrite it in simpler form as

$$\frac{dR}{dt} = \frac{K}{R} \left(\exp\left[\frac{-E_{\text{tot}}}{kT}\right] \right) \left(\exp\left[\frac{2\gamma_m\Omega}{kTR^*}\right] - \exp\left[\frac{2\gamma_m\Omega}{kTR}\right] \right), \quad (16b)$$

where $K = [(2 \sin \theta)(\nu_p)(\Omega)] / [(2 - 3 \cos \theta + \cos^3 \theta)(a)]$, and E_{tot} is the sum of all the activation energies in the expressions for c_p^{eq} , β , and β' : $E_{\text{tot}} = (\Delta H_{\text{sub}} - E_{\text{ad}}^s - H_{\text{ps}}) + H_{\text{ps}} + H_{\text{m}}^s = \Delta H_{\text{sub}} - E_{\text{ad}}^s + H_{\text{m}}^s$. Thus, E_{tot} is just the metal’s bulk sublimation enthalpy (ΔH_{sub}) minus the adsorption energy of a monomer on the support (E_{ad}^s) plus the diffusion activation energy of a metal monomer atom on the support (H_{m}^s). Importantly, neither E_{tot} nor Eq. (16b) includes the energy of the key intermediate (i.e., the monomer at the particle edge), since H_{ps} cancels in E_{tot} .

Note that Eq. (16) takes a very different form than Eq. (1) because we did not approximate the exponential term with just the first-order term in its Taylor series expansion as done by WG. We show below that higher-order terms are very important. In the equations above, γ_m could be defined by a single quantity that is appropriate for all island sizes as done by WG, but it could also be considered a function of R . Observations from recent adsorption microcalorimetric data in our group bring into serious question the assumption of constant surface free energy below 6 nm diameter,⁴³ which requires either treating γ_m as a function of R or using a different expression for the chemical potential of metal atoms in particles of radius R . We treat this issue next.

A. The chemical potential of a metal atom in a metal nanoparticle of radius R

The heat of adsorption of Pb atoms versus coverage on MgO(100) have been measured by Starr *et al.* at 300 K (Ref. 48) and ~ 150 K.⁴⁹ At both temperatures, the Pb atoms rapidly diffuse and form three-dimensional (3D) particles, with fewer, larger particles forming at 300 K. We used well-calibrated quantitative Auger spectroscopy data to estimate the average size of the Pb particles on the surface versus Pb coverage, and replotted the heat of adsorption versus Pb coverage as heat of adsorption versus average particle effective radius.⁴³ That plot is reproduced in Fig. 3. It assumes that the Pb particles are hemispherical caps, an assumption that is qualitatively supported by the contact angle estimated from their measured adhesion energy.⁴⁸

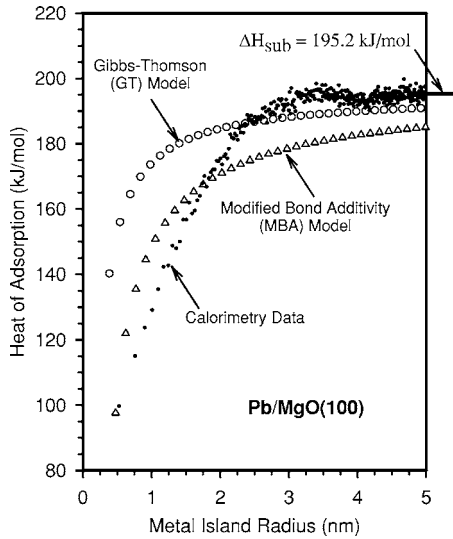


FIG. 3. A comparison between experimental microcalorimetry data for the heat of adsorption versus metal particle radius for Pb adsorption on Pb particles on MgO(100) and the two different theoretical models outlined in the text. The Gibbs-Thomson or GT model of Eq. (17) assumes that γ_m can be represented by a single value for all sizes of islands. This is seen to fit the experimental data very poorly at small radii. In contrast, the modified bond-additivity model or MBA model (see details in text) is a much better estimate for the experimental data.

Figure 3 also compares these measured energetics to those predicted by the GT relation, Eq. (8) above, assuming that the surface energy of Pb is equal to its bulk (large R) value, independent of radius. One can see the very poor agreement between this GT model and the calorimetric data below 3 nm radius. Here we have used for Pb's surface energy the value of $59 \mu\text{J}/\text{cm}^2$ reported by Tyson and Miller.⁵⁰ The more recent (and no doubt more accurate) value of $44 \mu\text{J}/\text{cm}^2$ reported by Bombis *et al.*⁵¹ would give even poorer agreement between this GT relation and the experimental data in Fig. 3.

Let us clarify the assumptions made in plotting the chemical potential of Eq. (8) on this adsorption enthalpy axis in Fig. 3. The GT relation states that the chemical potential (molar free energy) of a metal atom in a particle of radius R , $\mu(R)$, differs from that in an infinite radius particle, $\mu(\infty)$, by $\mu(R) - \mu(\infty) = (2\gamma_m\Omega)/R$, where γ_m is the surface free energy of the metal. Since there are only vibrational contributions to the entropy of these solid particles, and since the vibrational entropy of a solid metal makes a small contribution to its free energy compared to its enthalpy differences in Fig. 3, we can safely assume that the metal's entropy changes only negligibly with radius. Thus, we can equate this molar free energy (chemical potential) difference to the molar enthalpy difference, $H(R) - H(\infty)$, and thus to the difference in measured adsorption enthalpies, $-(\Delta H_{\text{ads}}(R) - \Delta H_{\text{ads}}(\infty))$, which we will refer to below as simply $E(R)$,

$$\mu(R) - \mu(\infty) = \frac{2\gamma_m\Omega}{R} = H(R) - H(\infty) = -[\Delta H_{\text{ads}}(R) - \Delta H_{\text{ads}}(\infty)] = E(R). \quad (17a)$$

The quantity $E(R)$, defined in Eq. (17), is just the difference

between the heat of metal atom adsorption onto hemispherical metal islands of radius R and the heat of adsorption onto the bulk metal (infinitely large islands), which is its bulk sublimation enthalpy [$\Delta H_{\text{sub}} = 195.2 \text{ kJ/mol}$ for solid Pb (Ref. 52)]. Rearranging Eq. (17) gives

$$\Delta H_{\text{ads}}(R) = \Delta H_{\text{sub}} - E(R) = \Delta H_{\text{sub}} - \frac{2\gamma_m\Omega}{R}. \quad (17b)$$

We calculated $\Delta H_{\text{ads}}(R)$ for the GT model in Fig. 3 using this expression, assuming that γ_m is independent of particle radius at its bulk value and using the bulk density of solid Pb ($11.4 \text{ g}/\text{cm}^3$) to get its atomic volume, Ω .

As written, Eq. (17) neglects the energy of the flat face of the hemisphere that touches the substrate, which for Fig. 3 is equivalent to setting the Pb/MgO(100) adhesion energy at this face equal to the Pb-Pb adhesion energy, or twice Pb's surface energy. This is a reasonable assumption, since the Pb/MgO(100) adhesion energy is $\sim 77 \mu\text{J}/\text{cm}^2$,⁴⁸ and Pb's surface energy is $44 \mu\text{J}/\text{cm}^2$.⁵¹ Nevertheless, this slightly underestimates the energy difference, $E(R)$. Including the Pb/MgO(100) adhesion energy of $77 \mu\text{J}/\text{cm}^2$ in this calculation would have the equivalent effect of changing the factor of 2 in Eqs. (8) and (17) to a 2.13. If the Pb/MgO(100) adhesion energy were instead zero, the lowest value it could possibly take, and included in Eqs. (8) and (17), it would be equivalent to changing the factor of 2 instead to 3. To make sure that we did not underestimate the magnitude of this surface energy correction in Fig. 3, we have used the older value of Pb's surface energy in making Fig. 3 [i.e., $59 \mu\text{J}/\text{cm}^2$ (Ref. 50)] instead of the much newer value [$44 \mu\text{J}/\text{cm}^2$ (Ref. 51)]. This is numerically equivalent to replacing the factor of 2 in Eqs. (8) and (17) with 2.67 but using the surface energy of $44 \mu\text{J}/\text{cm}^2$. This sets an upper limit on the correction needed to relax our neglect of the surface energy at the Pb/MgO(100) interface, and thus minimizes the disagreement between the GT model and the experimental data in Fig. 3.

Still, there is very poor agreement between the GT model and the calorimetric data seen in Fig. 3 for particles below 3 nm in radius (6 nm in diameter). This implies something very important about the surface free energy of the particles as grown on the surface: the surface free energy is *not* constant and instead increases strongly with decreasing radius of the islands below about 6 nm. For example, note that the measured heat of adsorption at $\sim 1 \text{ nm}$ radius (2 nm diameter) is $\sim 60 \text{ kJ/mol}$ smaller than expected if the surface energy is independent of particle radius.

The reason for this huge error is the fact that the surfaces of particles near 1 nm in radius have a larger fraction of high energy, coordinatively unsaturated metal atoms (i.e., at kinks, corners, etc.) than do very large particles (which are dominated by low surface energy facets). This is also the origin of the well-known difference in surface energies between different crystal faces.^{53,54} In agreement with the direction of our data, recent experimental measurements for free Ag nanoparticles suggested a surface energy that is sixfold higher than bulk Ag surfaces.⁵⁵ This is reminiscent of the

strong particle-size dependence of the melting point of clusters in this size range.^{56,57}

The magnitude of energy changes with radius in Fig. 3 highlights the error associated with neglecting the second- and higher-order terms in the Taylor expansions of Eqs. (9) and (10), as done by WG to get Eqs. (1) and (2). Neglecting these terms is equivalent to assuming that $\mu(R) - \mu(\infty)$ is small compared to kT . Inspection of the heat data in Fig. 3 proves that this is clearly not the case below 1000 K for particles smaller than 5 nm in diameter. Therefore, in the simulations below, we will use the more complex version of Eq. (16), which can be used for all temperatures and particle radii.

Figure 3 clearly shows that the assumption of constant γ_m when using Eq. (16b) above, as in the WG model, will lead to huge errors in the relative sintering rates of 1 nm versus 10 nm particles. To correct these errors, we recently introduced an approximation that gives radius-dependent chemical potentials for use in Eq. (16a), which are much closer to measured values,⁴³ as shown in Fig. 3. We call this approximation the “modified bond-additivity model” or “MBA model.” In this model, the energies of discrete, compact clusters were calculated, assuming nearest-neighbor bond additivity, setting all metal-metal bond energies equal to their bulk value (1/6 of the sublimation energy of the bulk solid Pb). Very stable cluster shapes were chosen by adding successive hexagonal close-packed layers in fcc packing (after the first two layers), with the number of atoms in each layer starting from the top given by: 1, 3, 7, 12, ... (i.e., each new underlayer providing a threefold hollow site for each atom in the layer above), as shown in Fig. 4. The effective radius, R , of each such cluster was calculated from its volume (V) assuming hemispherical shape: $V = \text{the number of atoms in a cluster} \times \Omega = 2\pi R^3/3$. The energies for other cluster sizes were assumed to vary linearly with radius between those computed for these very compact (pyramidal) clusters, thus modifying true bond-additivity, since surface atoms on less compact islands will clearly have a larger degree of coordinative unsaturation, and so their energies will be larger. For the MBA model in Fig. 3, the Pb-Pb bond energies were taken to equal 32.5 kJ/mol, or 1/6 of the sublimation energy of bulk, solid Pb, 195.2 kJ/mol.⁵² As can be seen, this MBA model gives a better approximation to the experimental data for small island sizes (<5 nm diameter) than does the GT relation. We explained previously⁴³ that errors associated with the assumptions in the MBA model roughly compensate, so that it gives reasonable agreement with the experimental heat data.

This agreement justifies use of this MBA model with other face-centered cubic (fcc) metals where the calorimetry data are not yet available (as we do below for gold), at least for qualitative understanding of the effect of their particle size on energy. We do this by scaling the particle energetics found for Pb (Fig. 3) by their metal-metal bond strength (or bulk sublimation energy), and scaling their effective radii by $\Omega^{1/3}$, both normalized to the values for Pb. Extrapolating in this way from Pb to other fcc metals, namely the noble and late transition metals, is justified by Yang and dePristo,⁵⁴ who showed that these fcc metals and Pb have a very similar relationship between a metal atom’s energy and its nearest-neighbor coordination number (CN).

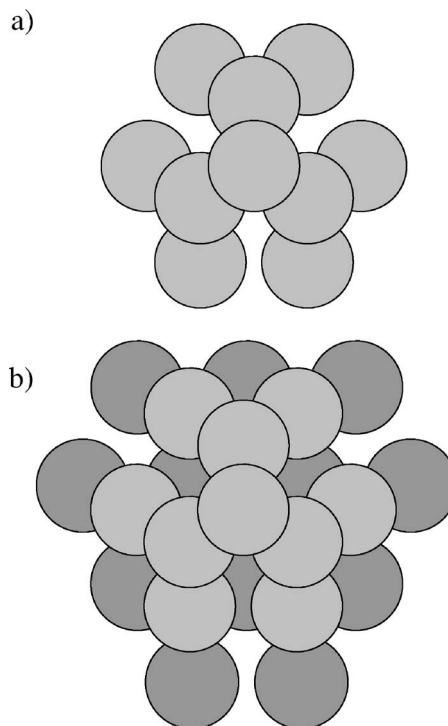


FIG. 4. The successive stacking of hexagonal close-packed layers in fcc packing, as used in the MBA model. (a) A metal island with 11 atoms as viewed from above. (b) A layer of atoms is added to the bottom of the existing island. One can count that 12 atoms (darker circles) must be added in order to preserve the pyramidal shape of the island. When adding these 12 atoms, 45 metal-metal bonds are formed.

Figure 5 shows the resulting energy versus particle size for Au nanoparticles calculated by this MBA model, and contrasts it with the predictions of the constant γ_m model (or GT model). Since the heat of sublimation of gold is

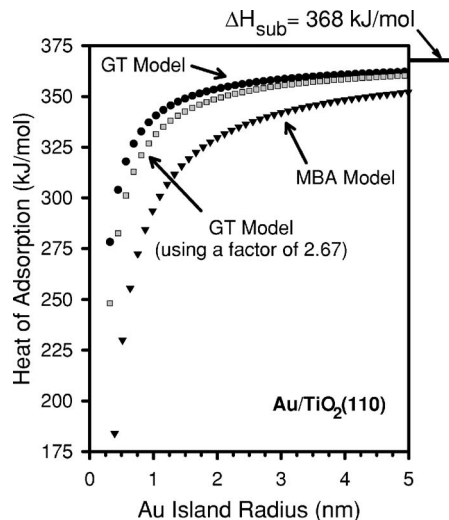


FIG. 5. A comparison of the heat of Au adsorption versus Au island size for Au islands on $\text{TiO}_2(110)$ calculated using the GT model, Eq. (17), and the modified bond-additivity (MBA) model. Also shown is the GT model where the factor of 2 in Eq. (17) was replaced with 2.67 (see text).

368 kJ/mol,⁵² the Au-Au bond energy is 1/6 of this for the MBA model, or 61.3 kJ/mol. The GT model in Fig. 5 uses the reported surface free energy of bulk solid Au of 140 $\mu\text{J}/\text{cm}^2$.^{50,58} (Egry *et al.* reported a value of 115 $\mu\text{J}/\text{cm}^2$ for liquid gold,⁵⁹ which is consistent with this value.⁵⁰) These energies will be used in simulating our measured kinetics for Au on $\text{TiO}_2(110)$ below. We also show in Fig. 5 the GT energies that would result if we replaced the factor of 2 in Eqs. (8) and (17) with 2.67, which sets an upper limit on the correction needed to compensate for this GT model's neglect of the surface energy of the flat face of the hemisphere that touches the substrate (see above). Relative to the large difference between the MBA and GT models, this is a very small effect, and will be neglected below.

The important quantity that we will need to take from Figs. 3 and 5 is $E(R)$, the difference between the heat of adsorption (chemical potential) for an island of radius R and that for the bulk (islands with infinite radius). One should notice that by using this MBA model for particles smaller than 4 nm in diameter, $E(R)$ becomes much larger than $2\gamma_m\Omega/R$ calculated using the bulk value of γ_m . This will dramatically affect the magnitude of dR/dt , which will in turn affect the temperature range over which the sintering of the films will occur. As an approximation, we will use this MBA model below to estimate the effect of the increase in free energy with decreasing radius on sintering kinetics.

B. Simulations of sintering kinetics during a linear temperature ramp

We first examine the effect of this change in $E(R)$ by comparing the predicted sintering kinetics of some model systems with and without this change using the interface control limit of the Ostwald ripening model. Using a radius-independent surface energy in this model gave Eq. (16) above, which we rewrite as follows (constant γ or GT model):

$$\frac{dR}{dt} = \frac{K}{R} \left(\exp\left[\frac{-E_{\text{tot}}}{kT}\right] \right) \left(\exp\left[\frac{2\gamma_m\Omega}{kTR^*}\right] - \exp\left[\frac{2\gamma_m\Omega}{kTR}\right] \right) \quad (18)$$

for direct comparison to the related expression obtained following the same derivation but without using the substitution of Eq. (8) (i.e., without the use of the GT relation),

$$\frac{dR}{dt} = \frac{K}{R} \left(\exp\left[\frac{-E_{\text{tot}}}{kT}\right] \right) \left(\exp\left[\frac{\mu(R^*) - \mu(\infty)}{kT}\right] - \exp\left[\frac{\mu(R) - \mu(\infty)}{kT}\right] \right), \quad (19a)$$

or the equivalent but simpler expression (general model) using $E(R)$ as defined above,

$$\frac{dR}{dt} = \frac{K}{R} \left(\exp\left[\frac{-E_{\text{tot}}}{kT}\right] \right) \left(\exp\left[\frac{E(R^*)}{kT}\right] - \exp\left[\frac{E(R)}{kT}\right] \right). \quad (19b)$$

We will use the MBA model to calculate $E(R)$ in Eq. (19b).

A computer program that starts with a Gaussian distribution of islands sizes was written to propagate these differential equations in time by finite-difference methods. By raising the temperature a tiny amount ($B^*\Delta t$) at each time step, where B is the heating rate, we used this program to model a typical TP-LEIS measurement at constant heating rate ($B = 1 \text{ K/s}$). Note that $E_{\text{tot}} = \Delta H_{\text{sub}} - E_{\text{ad}}^s + H_m^s$ and

$$K = \frac{\sin(\theta)\nu_p\Omega}{2\alpha_1 a}$$

are the only adjustable parameters in using Eqs. (18) and (19). Since diffusion energies are typically 10 to 40% of adsorption energies,^{60–62} and since density function theory (DFT) calculations for Pd on $\text{MgO}(100)$ gave a diffusion barrier that is 25% of its adsorption energy,^{63,64} we will take H_m^s to be 0.25 E_{ad}^s below. This simplifies E_{tot} to $E_{\text{tot}} = \Delta H_{\text{sub}} - 0.75E_{\text{ad}}^s$. Instead of quoting the value of K that was used below, we will quote the value of ν_p instead. This prefactor will generally be taken to be 10^{12} to 10^{14} s^{-1} , typical values found for such processes.^{36,60,63–65} The only other adjustable parameter in K is θ , the contact angle, which we have assumed to be $\theta = 90^\circ$ in the simulations below. Unless θ gets very small, it only weakly affects K , and in any case can be compensated by changing the parameter ν_p . Changing θ from 90° to 45° increases K by a factor of 6, so decreasing ν_p sixfold would compensate for this.

We will use the sintering of Pb particles on $\text{MgO}(100)$ as an example system to show the effects on kinetics of initial island size distributions, kinetic parameters, and choice of $E(R)$ model. For this system, we first take $\nu_p = 6 \times 10^{12} \text{ s}^{-1}$ and $E_{\text{tot}} = 141 \text{ kJ/mol}$. Since $\Delta H_{\text{sub}} = 196 \text{ kJ/mol}$ for Pb, this value of $E_{\text{tot}} (= \sim \Delta H_{\text{sub}} - 0.75E_{\text{ad}}^s)$ implies that $E_{\text{ad}}^s = \sim 73 \text{ kJ/mol}$. This adsorption energy equals that estimated from the surface residence time of Pb adatoms on $\text{MgO}(100)$ at 280 K measured here⁶⁶ using the apparatus and procedure described in Ref. 67. (This estimate assumed a prefactor for desorption of $4 \times 10^{14} \text{ s}^{-1}$.)

Figure 6 shows a direct comparison of the sintering kinetics within the GT and MBA models for Pb/ $\text{MgO}(100)$. In these plots, we have again estimated $E_{\text{tot}} = 141 \text{ kJ/mol}$ and $\nu_p = 6 \times 10^{12} \text{ s}^{-1}$. The initial radii of the particles are given by a Gaussian distribution with $\langle R \rangle = 0.6 \text{ nm}$, and the full width at half maximum (FWHM) of the distribution was 0.2 nm. From this figure, it is quite obvious that the MBA model markedly expands the range over which Ostwald ripening occurs to lower temperatures. This temperature range is twice as wide in absolute temperature. This broader temperature range is required because of the dramatic decrease in metal atom stability for the small particles initially present (Fig. 3).

Figure 7 shows directly the effect of changing the initial average radii of the particles. The FWHM of the particle distributions was held constant at 0.2 nm. Four different values of $\langle R \rangle$ are plotted: 1.1 nm, 2.1 nm, 3.1 nm, and 8.1 nm. Again, $E_{\text{tot}} = 141 \text{ kJ/mol}$ and $\nu_p = 6 \times 10^{12} \text{ s}^{-1}$. As can be seen, when $\langle R \rangle$ gets smaller, the onset temperature for Ostwald ripening decreases dramatically to lower temperatures. Again, this is directly related to Fig. 3.

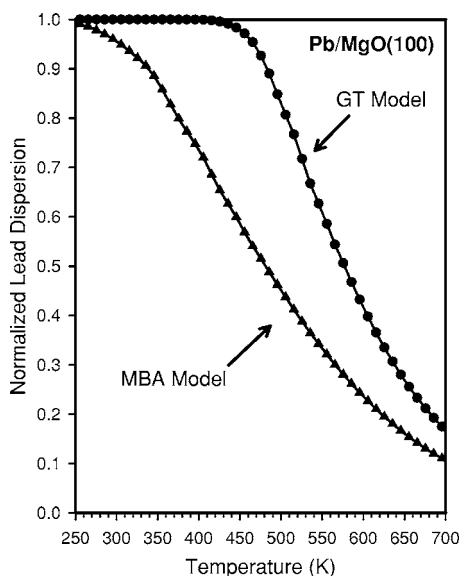


FIG. 6. A comparison of the Ostwald ripening of Pb particles on MgO(100) when heated at 1 K/s, within the GT model and the MBA model, assuming $E_{tot}=141$ kJ/mol (see text) and $\nu_p=6 \times 10^{12}$ s $^{-1}$. The initial island size distribution had a mean radius of $\langle R \rangle=0.6$ nm and had the same FWHM of 0.2 nm. The temperature range of sintering is shown to be much broader for the MBA model.

We also tested the effect of the width of the initial island size distributions on sintering kinetics within the MBA model. The mean radii of these distributions were held constant at $\langle R \rangle=3.1$ nm, but the FWHM was varied from 1.7 nm to 0.2 nm. The onset of the sintering occurred slightly earlier for the wider island size distribution, since it includes smaller islands that will ripen at lower temperatures. Once

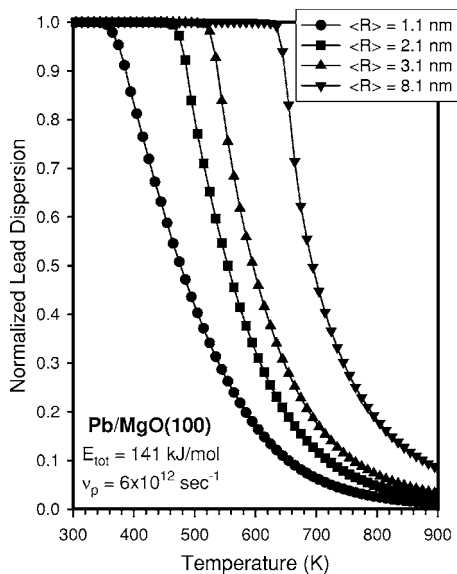


FIG. 7. Ostwald ripening of Pb particles on MgO(100) when heated at 1 K/s, as predicted by the MBA model for island size distributions of different initial mean radii, assuming $E_{tot}=141$ kJ/mol (see text) and $\nu_p=6 \times 10^{12}$ s $^{-1}$. The distributions all had the same FWHM of 0.2 nm. The distributions that included islands with smaller radii began to thicken at a lower temperature.

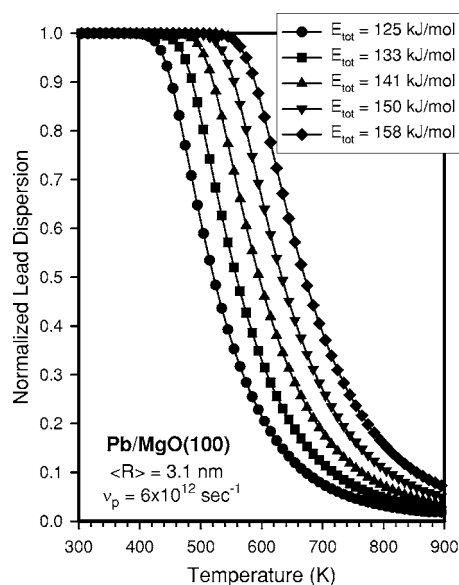


FIG. 8. Ostwald ripening of Pb particles on MgO(100) when heated at 1 K/s, as predicted by the MBA model while varying the energetic parameter E_{tot} . The initial size distributions all had the same mean radius of $\langle R \rangle=3.1$ nm and FWHM of 1.7 nm.

these smaller islands have sintered, though, the films all thickened at nearly the same rate.

Figure 8 shows the effect of E_{tot} . The mean radius of the distribution is fixed for all the plots at $\langle R \rangle=3.1$ nm and $\nu_p=6 \times 10^{12}$ s $^{-1}$, while E_{tot} is varied between 125 kJ/mol and 158 kJ/mol. Decreasing E_{tot} decreases the mean temperature at which the film sinters. The width of the temperature range of the sintering does not change dramatically, only the average temperature at which the film ripens.

Figure 9 shows the result of varying the prefactor ν_p . When varying the prefactor over four orders of magnitude,

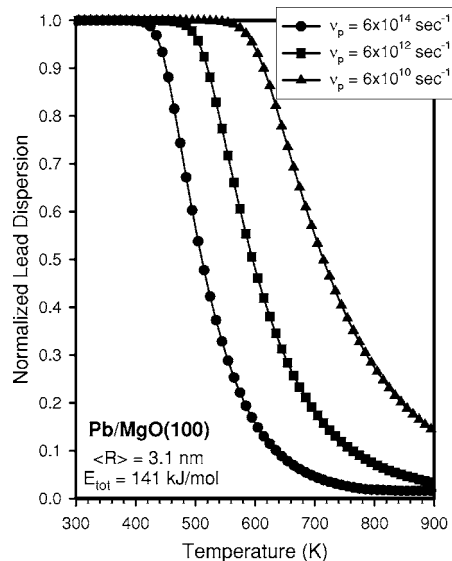


FIG. 9. Ostwald ripening of Pb particles on MgO(100) when heated at 1 K/s, as predicted by the MBA model, for different values of the prefactor ν_p . The initial size distributions all had the same mean radius of $\langle R \rangle=3.1$ nm FWHM of 1.7 nm.

the mean temperature at which the film sinters changes by ~ 200 K. The other parameters ($E_{\text{tot}}=141$ kJ/mol and $\langle R \rangle = 3.1$ nm) were held constant here. The temperature range of thickening also narrows as ν_p increases.

C. Kinetics of Ostwald ripening in other regimes and of particle diffusion/coalescence

The treatment of sintering kinetics by WG (Refs. 1–3) covered a number of other kinetic limits of the Ostwald-ripening mechanism beyond the “interface-controlled” limit discussed above. Since the factor $e^{\{\mu(R)-\mu(\infty)\}/kT}$ also appears in those rate expressions, it is also very important to include in them a proper treatment of the dramatic particle-size effect on $\mu(R)$ mentioned above. This could be included in an approximate way using the MBA model described above, and should provide a dramatic improvement for particles smaller than 6 nm in diameter.

It is equally important to properly treat this dramatic particle-size effect on metal atom energy in kinetic models for sintering mechanisms dominated by particle diffusion/agglomeration instead of Ostwald ripening. This is because the factor $e^{\{\mu(R)-\mu(\infty)\}/kT}$ also appears directly in the rate expression for sintering by that mechanism, at least when the particle diffusion mechanism requires monomer diffusion around the perimeter of the particle.^{13,14} This arises from the particle-size dependence of the diffusion rate constant for particle diffusion across the oxide, which has been written as^{13,14}:

$$D(R) = \frac{3\Omega^2}{\pi R^4} D_{c\infty} \exp\left[\frac{\mu(R) - \mu(\infty)}{kT}\right], \quad (20)$$

where D is a constant. It is clear from Fig. 3 that one cannot neglect the particle-size effect in the surface energy (i.e., assume the surface energy is a constant) when calculating $\mu(R)$ in this equation. Since this size effect is huge (see above) and enters in the resulting kinetic equations in an Arrhenius-like form (i.e., exponentially), it is a very serious error for small particle sizes. Again, using the MBA model should provide a much better approximation and should improve substantially any kinetic model based on this equation.

We next show that use of the MBA model greatly improves the agreement between experimental measurements of sintering kinetics and simulations, for a system where the Ostwald ripening mechanism dominates.

D. Measured and simulated sintering kinetics of Au nanoparticles on TiO₂(110)

Figure 10 shows TP-LEIS measurements of the sintering kinetics of Au nanoparticles on TiO₂(110) at 300 K, with a heating rate of 1.0 K/s, for three different total Au coverages between 0.13 to 0.75 ML. The Au was vapor deposited in ultrahigh vacuum on the clean, stoichiometric TiO₂(110) surface, which results in nanoparticles of Au, as shown previously.⁴⁵ LEIS directly measures the fraction of the surface covered by metal islands, thus providing the same measure of metal dispersion as simulated in Figs. 6–9 above. The resulting TP-LEIS measurements for all coverages show that

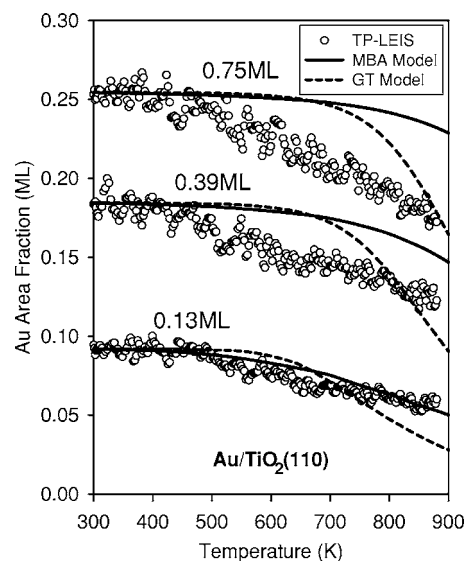


FIG. 10. A comparison of experimental TP-LEIS data (at a heating rate of 1 K/s) for Au particles on TiO₂(110) with the MBA and GT Ostwald ripening models. The Au coverages are in units of ML, where 1 ML is defined as the Au(111) packing density, 1.39×10^{15} atoms/cm². For all simulations, $E_{\text{tot}}=327$ kJ/mol in the MBA model and 240 kJ/mol in the GT model. Initial size distributions and prefactors were, from the bottom curve up, 0.13 ML: $\langle R \rangle = 0.45$ nm, FWHM=0.20 nm, $\nu_p = 4 \times 10^{12}$ s⁻¹; 0.39 ML: $\langle R \rangle = 0.64$ nm, FWHM=0.60 nm, $\nu_p = 4 \times 10^{12}$ s⁻¹; and 0.75 ML: $\langle R \rangle = 0.75$ nm, FWHM=1.15 nm, $\nu_p = 4 \times 10^{12}$ s⁻¹.

sintering starts below ~ 400 K and continues with a nearly constant rate of decrease in the Au area fraction until ~ 900 K. The lowest coverage result has been presented previously.⁴³

We now argue that the Au dispersion is proportional to this Au TP-LEIS signal, and both are inversely proportional to the average Au particle radius. Dispersion is defined as the fraction of the Au atoms that are on the exposed particles' surfaces, so it is proportional to the area:volume ratio of the gold. This is the product of the Au area per particle (a_{Au}) times the number density of particles (N =number per unit substrate area), divided by the Au volume per unit substrate area. We assume that the total volume of Au remains constant (i.e., no significant loss of Au from the surface region during TP-LEIS). This is justified by the fact that Au desorption was not observed (with a line-of-sight mass spectrometer) below 900 K. Also, Mitchell *et al.*²¹ concluded that desorption does not compete with sintering until above 873 K for this system. Therefore, Au dispersion is proportional to a_{Au} times N . We further assume that the Au particles retain a fixed shape of either hemispheres or cylindrical discs of fixed thickness-to-diameter ratio, so that a_{Au} is proportional to particle radius squared, and N is inversely proportional to the volume per particle (or particle radius cubed). Thus, dispersion is inversely proportional to radius, R . The Au LEIS signal is proportional to N times the area per Au particle projected onto the substrate surface, πR^2 , so the Au LEIS signal also is inversely proportional to radius. Therefore, the Au dispersion is proportional to the LEIS signal. The observed linear decrease in Au TP-LEIS signal with

time (temperature) in Fig. 10 thus indicates that the Au dispersion decreases linearly with time, that the average Au particle radius increases linearly with time, and that the number density of Au particles decreases as time cubed.

We now try to use the Ostwald ripening kinetic model, coupled with the metal energy versus particle size discussed above, to simulate these TP-LEIS data. Note that Ostwald ripening is thought to be the dominant mechanism for sintering of Au on TiO₂(110) under conditions like those here where the main sintering occurs (500–900 K in UHV).^{12,21,22} The numerical simulations were performed as described above, using Eq. (19) for the MBA model and, for comparison, Eq. (18) for the GT model. The energy versus Au particle size, $E(R)$, for the MBA model used was shown in Fig. 5.

The adjustable parameters needed for this simulation are the initial island size distribution, their contact angle θ , E_{tot} , and ν_p . Large gold clusters on TiO₂(110) were estimated to have an equilibrium contact angle of 120°,¹⁵ but small clusters should have a smaller contact angle,^{68,69} so we estimated $\theta=90^\circ$ (i.e., hemispherical particles) here and did not adjust it further. Once the hemispherical island shape is assumed, two relations were used to estimate the average initial Au particle radius (R_{av}) and particle number density: (1) the measured initial LEIS Au area fraction (0.095 at this coverage) equals the average particle area (πR_{av}^2) times their number density. (2) The island volume ($2/3\pi R_{\text{av}}^3$) times their number density equals the total Au coverage of 0.13 times the thickness on one Au ML of 0.235 nm.⁴⁵ These were used to estimate a particle radius of 0.45 nm and number density of $1.4 \times 10^{13}/\text{cm}^2$. The average initial radius of Au clusters grown on TiO₂(110) at similar coverage and deposition conditions was estimated by (STM) (Ref. 12) and high-resolution scanning electron microscopy (HRSEM) (Ref. 15) to be about 1 nm. The average radius estimated from the LEIS data here is slightly smaller, possibly because those techniques would have missed the smallest particles. The number density of islands does not affect the sintering rates within this “interface-control” model, which assumes that monomer diffusion on the oxide is fast compared to detachment from island edges. We assumed that the as-deposited Au islands had a Gaussian distribution of radii, with the average being 0.45 nm as estimated above, and with a FWHM of 0.20 nm.

At the two higher Au coverages in Fig. 10 (0.39 and 0.75 ML), the measured initial LEIS Au area fractions (0.18 and 0.25, respectively) were used to estimate the initial average particle sizes, assuming that the initial number density of Au particles at 300 K is the same as at the lower coverage ($1.4 \times 10^{13}/\text{cm}^2$). During growth of Au on stoichiometric TiO₂(110) at 300 K, the number density of islands stays fairly constant with coverage in this range.^{12,15} Again, the particles were assumed to be hemispherical caps. This gave average island radii of 0.64 and 0.75 nm, respectively. Note that these radii and island densities are also consistent with the total Au coverages, within experimental error, verifying the assumption that the initial number density of islands was nearly independent of total Au coverage. It was further assumed that the width of the initial particle radii distributions

increased proportional to the total Au coverage, from the value of 0.20 nm at 0.13 ML. This gives widths (FWHM) of 0.60 and 1.15 nm at 0.39 and 0.75 ML, respectively.

The parameters E_{tot} and ν_p were adjusted to get a reasonable fit of the simulation to the lowest coverage TP-LEIS data. Figure 10 shows the resulting fits within the MBA and the GT models. Each fit is not the “best” fit of the data. Rather, it is meant to show that with a reasonable set of parameters, one can reasonably well fit and correctly model the very broad range of temperatures over which the catalyst ripens with nearly constant rate using the MBA model (but not with the GT model). These fits for the lowest coverage curve have been presented previously.⁴³

The adjustable parameters used in this MBA model were physically reasonable too: $E_{\text{tot}}=327$ kJ/mol and $\nu_p=4 \times 10^{12}$ s⁻¹. Prefactors for metal atom migration steps on surfaces (ν_p) are typically found to be 10^{12} – 10^{14} s⁻¹.^{36,60–63,65} Because ΔH_{sub} for gold is 368 kJ/mol,⁵² the best-fit value of E_{tot} (327 kJ/mol) implies that $E_{\text{ad}}^s - H_m^s$ is 41 kJ/mol, which is also quite reasonable given that E_{ad}^s for Au on alumina was estimated to be ~ 30 kJ/mol by modeling of nucleation kinetics,⁷⁰ that the diffusion activation energy of a metal monomer on the support (H_m^s) is small, and that DFT calculations give a value of ~ 56 kJ/mol for Au on TiO₂(110).⁷¹

As discussed previously,⁴³ the GT model does not fit this lowest coverage data as well. More importantly, the parameters needed for the GT fit are not reasonable. For example, the value of E_{tot} (240 kJ/mol) implies that $E_{\text{ad}}^s - H_m^s$ is 128 kJ/mol, which is clearly larger than even E_{ad}^s (see above). The GT model could not be made to fit the data significantly better with more reasonable parameters.

Figure 10 also shows the simulations of TP-LEIS for the two higher initial Au coverages, assuming the same values for these parameters in both the MBA and the GT models as used to fit the lowest-coverage data. These parameters do a poor job of fitting these higher-coverage data in both models.

As shown in Fig. 11, the higher-coverage data can be well fitted with the MBA model if we assume that ν_p remains constant at its low-coverage value (4×10^{12} s⁻¹), but that E_{tot} decreases below the low-coverage fit value of 327 kJ/mol, to 293 and 280 kJ/mol, for coverages of 0.39 and 0.75 ML, respectively. A higher effective value of E_{tot} at lower Au coverage is actually expected, since the metal atoms in the smaller islands (at lower coverage) feel more stabilization by defect sites on the oxide surface. Metal islands are well known to be stabilized by and nucleate at surface defects such as oxygen vacancies and steps,^{11,64,72–75} particularly for Au on TiO₂(110).^{37,76–78} At lower coverage, the metal atoms in islands are, on average, more affected by defects. The model above does not explicitly consider the effect of such defects, and so it is expected that some minor increase in E_{tot} with decreasing coverage should be necessary.

As also shown in Fig. 11, the corresponding GT model gives a poorer fit to the higher coverage data even when E_{tot} is allowed to vary to achieve the best fit. Again, this highlights the importance of the better estimation on the particle-size dependence of the metal chemical potential in the MBA model.

We also performed simulations like those in Fig. 11 but wherein we assumed that the initial particle-size distributions

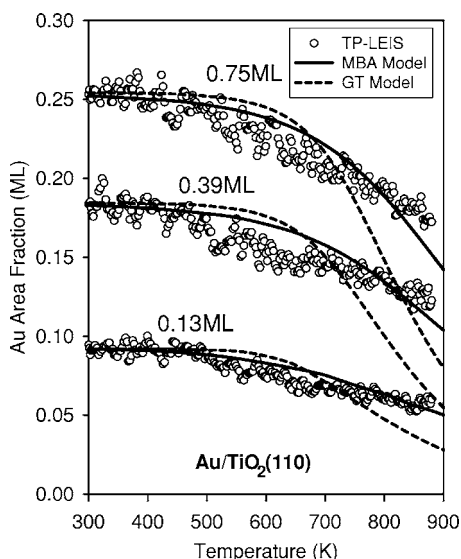


FIG. 11. A comparison of experimental TP-LEIS data (at 1 K/s) for Au particles on $\text{TiO}_2(110)$ with the MBA and GT Ostwald ripening models. Same parameters as Fig. 10, except here the MBA and GT fits at the two higher coverages were improved by allowing E_{tot} to be adjusted as a fit parameter (since it should decrease with coverage due to the decreasing role of defect sites). Best fit values were, from the bottom curve up, 0.13 ML: $E_{\text{tot}}=327$ kJ/mol (MBA) and 240 kJ/mol (GT); 0.39 ML: $E_{\text{tot}}=287$ kJ/mol (MBA) and 220 kJ/mol (GT); and 0.75 ML: $E_{\text{tot}}=263$ kJ/mol (MBA) and 210 kJ/mol (GT).

were Gaussian in volume (rather than in radius). This broadens these radius distributions to smaller radii, which resulted in a slightly better fits to the data at all three coverages than shown in Fig. 11, while at the same time requiring less variation in E_{tot} (now only from 327 to 300 kJ/mol with increasing coverage).

To simplify the models, we have ignored above the effect of a known tendency for Au islands on $\text{TiO}_2(110)$ to thicken without any increase in volume per island (i.e., to evolve toward an equilibrium shape) as temperature is increased.^{15,79} We assumed here that the islands already start out in their equilibrium shape.

We now address the implications of these models with respect to long-term sintering predictions for an initial Au coverage of 0.13 ML. In practice during industrial catalyst development, one would hope to use a kinetic model to simulate the short-term sintering data, and hope that it makes a good prediction for long, industrially relevant times, like 1 yr. We treat Figs. 10 and 11 as the “short-term” simulation here, and use its resulting fit parameters to predict sintering for 1 yr at 700 K. Note that both the best-fit MBA and GT model give nearly the same dispersion after the short-term sintering to 700 K (Fig. 11). The results of stopping the heating ramp at 700 K and then holding the temperature at 700 K for 1 yr are shown in Fig. 12. As can be seen, the dispersion predicted by the GT model decreases to only 30% of that predicted by the MBA model. More importantly, the resulting average particle size increases to over 9 nm diameter after 1 yr in the GT simulation, whereas it remains below 3 nm in the MBA simulation, as shown in the resulting

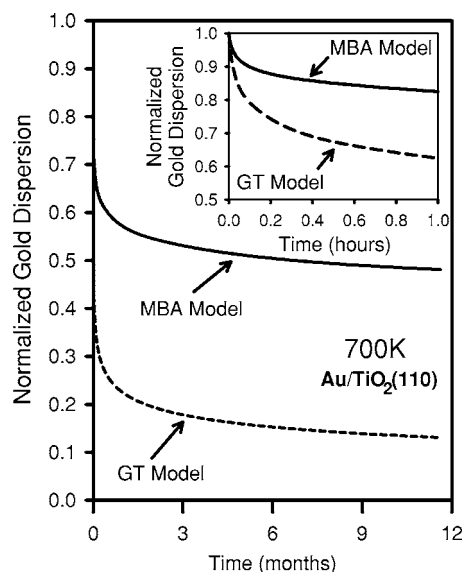


FIG. 12. Predictions of the Au particle dispersion versus time within the MBA and GT models for the long-term sintering of 0.13 ML of Au on $\text{TiO}_2(110)$ at 700 K. Same parameters used as obtained from fitting the short-term data (i.e., the bottom curves in Figs. 10 and 11 that were fitted to experimental TP-LEIS data).

particle size distributions in Figs. 13 and 14. This is a dramatic difference, given the fact that 3 nm Au particles on TiO_2 are very active in low-temperature CO oxidation but 6 nm particles are nearly dead.^{37,38} If one were trying to use such simulations to guide industrial research, the GT prediction would cause one to conclude that this is a bad catalyst not worthy of further research, whereas the MBA prediction would give one great hope for this catalyst. This again highlights the importance of this new, more energetically correct kinetic model.

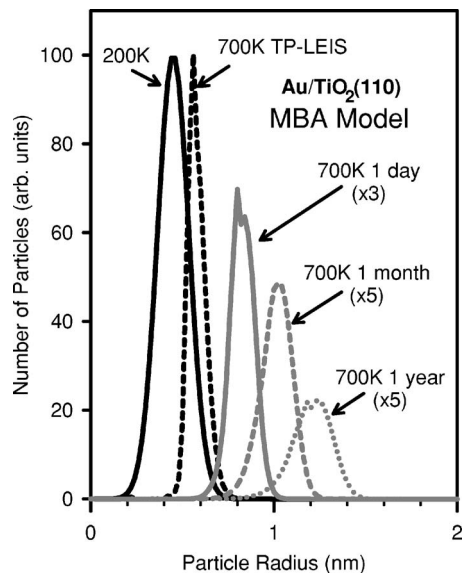


FIG. 13. Predictions by the MBA model of the Au particle size distributions for 0.13 ML of Au on $\text{TiO}_2(110)$ after sintering at 700 K for different times up to 1 yr. Same parameters as Fig. 12 and the bottom curve in Figs. 10 and 11.

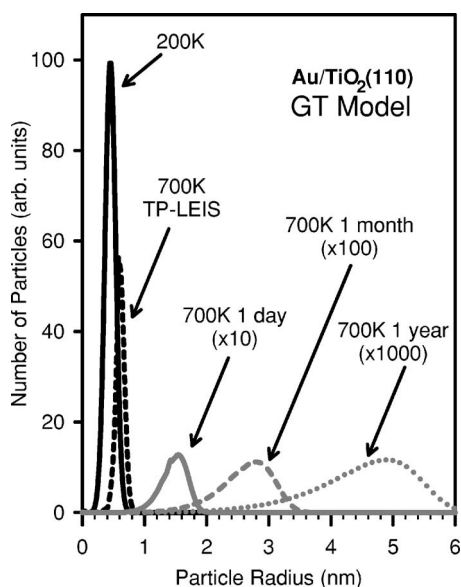


FIG. 14. Predictions by the GT model of the Au particle size distributions for 0.13 ML of Au on $\text{TiO}_2(110)$ after sintering at 700 K for different times up to 1 yr. Same parameters as Fig. 12 and the bottom curve in Figs. 10 and 11.

The particle size distributions in Figs. 13 and 14 show that the initial Gaussian distribution broadens with time and becomes asymmetric, with greater width on the lower-radius side of the maximum in both models. The width of the distribution is predicted with the MBA model to broaden much less compared to the GT model, for the same extent of sintering (i.e., for different times that result in the same final average radii).

These size distributions show that there are serious problems with the widely used classical method for determining the sintering mechanism based solely upon the shape of the sintered particle-size distribution. Basically, that method claims that the distribution is log-normal (i.e., has a sharp leading edge and a long tail to larger sizes) if the sintering occurs by particle diffusion/coalescence whereas it has a long tail to small sizes and a sharp trailing edge when sin-

tering occurs by Ostwald ripening.^{80–82} One can see that is not true when one includes the proper kinetic rate laws and particle-size dependent energetics. The derivation of the log-normal distribution assumes that the probability that two particles agglomerate is independent of their size.^{80,81} This is clearly not the case, since Eq. (20) implies a very strong particle-size dependence. Thus, we conclude that, in this size range below 6–10 nm in diameter, one cannot use the shape of the particle-size distribution to determine sintering mechanisms. This is consistent with a recent study of sintering mechanisms and particle-size distributions using electron microscopy by Datye *et al.*¹⁹

IV. CONCLUSIONS

We have used TP-LEIS to study the sintering of Au particles on $\text{TiO}_2(110)$. The temperature range for sintering was experimentally found to be much broader than could be explained by earlier Ostwald ripening kinetic models. We have derived kinetic equations for sintering that include more accurate particle-size dependent energetics, based on microcalorimetric data for the heat of adsorption of a metal on an oxide substrate. With this model, the temperature range of ripening could be broadened such that it accurately corresponds to the experimental data. This kinetic model for Ostwald ripening accomplishes this using physically reasonable parameters. We therefore expect that this model will be much better for predicting long-term isothermal sintering kinetics of catalysts based on short-term measurements. This could have a positive impact on testing and development of new catalysts.

ACKNOWLEDGMENTS

Support for this work by the U.S. Department of Energy, Office of Basic Energy Sciences, Chemical Sciences Division, Grant No. DE-FG02-96ER14630 is gratefully acknowledged. The authors thank Lien Ngo, Abhaya Datye, Wayne Goodman, Claude Henry, John Venables, Zbigniew Lodziana, Nicholas Bailey, Thomas Bligaard, and David Starr for enlightening discussions.

*Corresponding author.

¹P. Wynblatt and N. A. Gjostein, *Prog. Solid State Chem.*, edited by J. O. McCaldin and G. A. Somorjai Elsevier Science, Amsterdam, 1975), Vol. (9), p. 21.

²P. Wynblatt, R. A. D. Betta, and N. A. Gjostein, in *The Physical Basis for Heterogeneous Catalysis*, edited by E. Drauglis and R. I. Jaffee (Plenum Press, New York, 1975), p. 501.

³P. Wynblatt and N. A. Gjostein, *Acta Metall.* **24**, 1165 (1976).

⁴T.-H. Ahn, P. Wynnblatt, and J. K. Tien, *Acta Metall.* **29**, 921 (1981).

⁵G. B. McVicker, R. L. Garten, and R. T. Baker, *J. Catal.* **54**, 129 (1978).

⁶E. Ruckenstein and D. B. Dadyburjor, *Rev. Chem. Eng.* **1**, 251 (1983).

⁷G. A. Fuentes and E. D. Gamas, in *Catalyst Deactivation*, edited by C. H. Bartholomew and J. B. Butt (Elsevier Science, Amsterdam, 1991), p. 637.

⁸G. A. Fuentes and E. Salinas-Rodriguez, in *Catalyst Deactivation*, edited by C. H. Bartholomew and G. A. Fuentes (Elsevier Science, Amsterdam, 1997), p. 573.

⁹C. H. Bartholomew, in *Catalyst Deactivation 1994*, edited by B. Delmon and G. F. Froment, Vol. Studies in Surface Science and Catalysis 88 (Elsevier Science B.V., Amsterdam, 1994).

¹⁰C. H. Bartholomew, in *Catalyst Deactivation*, edited by C. H. Bartholomew and G. A. Fuentes (Elsevier Science B.V., Amsterdam, 1997), p. 585.

¹¹C. T. Campbell, *Surf. Sci. Rep.* **227**, 1 (1997).

- ¹²X. Lai and D. W. Goodman, *J. Mol. Catal. A: Chem.* **162**, 33 (2000).
- ¹³M. J. Jak, C. Konstapel, A. v. Kreuningen, J. Crost, J. Verhoeven, and J. W. Frenken, *Surf. Sci.* **474**, 28 (2001).
- ¹⁴M. J. Jak, C. Konstapel, A. v. Kreuningen, J. Verhoeven, and J. W. Frenken, *Surf. Sci.* **457**, 259 (2000).
- ¹⁵F. Cosandey and T. E. Madey, *Surf. Rev. Lett.* **8**, 73 (2001).
- ¹⁶A. G. Sault and V. Tikare, *J. Catal.* **211**, 19 (2002).
- ¹⁷J. Sehested, *J. Catal.* **217**, 417 (2003).
- ¹⁸A. Imre, E. Gontier-Moya, D. L. Beke, I. A. Szabo, and G. Erdelyi, *Surf. Sci.* **441**, 133 (1999).
- ¹⁹A. K. Datye, Q. Xu, K. C. Kharas, and J. M. McCarty, *Catal. Today* **111**, 59 (2006).
- ²⁰Q. Xu, K. C. C. Kharas, and A. K. Datye, in *Catalyst Deactivation 2001*, edited by J. J. Spivey, G. W. Roberts, and B. H. Davis (Elsevier Science, Amsterdam, 2001), p. 157.
- ²¹C. E. J. Mitchell, A. Howard, M. Carney, and R. G. Egdell, *Surf. Sci.* **490**, 196 (2001).
- ²²A. Kolmakov and D. W. Goodman, *Catal. Lett.* **70**, 93 (2000).
- ²³S. Kielbassa, M. Kinne, and R. J. Behm, *J. Phys. Chem. B* **108**, 19184 (2004).
- ²⁴E. C. H. Sykes, F. J. Williams, M. S. Tikhov, and R. M. Lambert, *J. Phys. Chem. B* **106**, 5390 (2002).
- ²⁵A. Kolmakov and D. W. Goodman, *Chem. Rec.* **2**, 446 (2002).
- ²⁶A. Howard, C. E. J. Mitchell, and R. G. Egdell, *Surf. Sci.* **515**, L504 (2002).
- ²⁷J. Sehested, J. A. P. Gelten, and S. Helveg, *Appl. Catal., A* **309**, 237 (2006).
- ²⁸W. F. Yan, S. Brown, Z. W. Pan, S. M. Mahurin, S. H. Overbury, and S. Dai, *Angew. Chem., Int. Ed.* **45**, 3614 (2006).
- ²⁹T. Okazawa, M. Fujiwara, T. Nishimura, T. Akita, M. Kohyama, and Y. Kido, *Surf. Sci.* **600**, 1331 (2006).
- ³⁰Y. Maeda, T. Fujitani, S. Tsubota, and M. Haruta, *Surf. Sci.* **562**, 1 (2004).
- ³¹F. B. Rasmussen, J. Sehested, H. T. Teunissen, A. M. Molenbroek, and B. S. Clausen, *Appl. Catal., A* **267**, 165 (2004).
- ³²J. Sehested, J. A. P. Gelten, I. N. Remediakis, H. Bengaard, and J. K. Norskov, *J. Catal.* **223**, 432 (2004).
- ³³A. Imre, D. L. Beke, E. Gontier-Moya, I. A. Szabo, and E. Gillet, *Appl. Phys. A: Mater. Sci. Process.* **71**, 19 (2000).
- ³⁴G. Mills, T. R. Mattsson, L. Mollnitz, and H. Metiu, *J. Chem. Phys.* **111**, 8639 (1999).
- ³⁵T. R. Mattsson, G. Mills, and H. Metiu, *J. Chem. Phys.* **110**, 12151 (1999).
- ³⁶L. Bardotti, P. Jensen, A. Hoareau, M. Treilleux, B. Cabaud, A. Perez, and F. C. S. Aires, *Surf. Sci.* **367**, 276 (1996).
- ³⁷M. Valden, X. Lai, and D. W. Goodman, *Science* **281**, 1647 (1998).
- ³⁸M. Valden, S. Pak, X. Lai, and D. W. Goodman, *Catal. Lett.* **56**, 7 (1998).
- ³⁹M. Haruta, *Catal. Today* **36**, 153 (1997).
- ⁴⁰M. Haruta, *Cattech* **6**, 102 (2002).
- ⁴¹D. W. Goodman, *Catal. Lett.* **99**, 1 (2005).
- ⁴²S. L. Tait, L. T. Ngo, Q. M. Yu, S. C. Fain, and C. T. Campbell, *J. Chem. Phys.* **122**, 064712(2005).
- ⁴³C. T. Campbell, S. C. Parker, and D. E. Starr, *Science* **298**, 811 (2002).
- ⁴⁴L. Gamble, L. S. Jung, and C. T. Campbell, *Surf. Sci.* **348**, 1 (1996).
- ⁴⁵S. C. Parker, A. W. Grant, V. A. Bondzie, and C. T. Campbell, *Surf. Sci.* **441**, 10 (1999).
- ⁴⁶J. Yoshihara, J. M. Campbell, and C. T. Campbell, *Surf. Sci.* **406**, 235 (1998).
- ⁴⁷P. Atkins, *Physical Chemistry* (W. H. Freeman, New York, 1998).
- ⁴⁸D. E. Starr, D. J. Bald, J. Musgrove, J. Ranney, and C. T. Campbell, *J. Chem. Phys.* **114**, 3752 (2001).
- ⁴⁹D. E. Starr and C. T. Campbell, *J. Phys. Chem. B* **105**, 3776 (2001).
- ⁵⁰W. R. Tyson and W. A. Miller, *Surf. Sci.* **62**, 267 (1977).
- ⁵¹C. Bombis, A. Emundts, M. Nowicki, and H. P. Bonzel, *Surf. Sci.* **511**, 83 (2002).
- ⁵²D. R. Lide, Ed., *CRC Handbook of Chemistry and Physics* (CRC Press, Boston, MA, 1996).
- ⁵³M. Methfessel, D. Hennig, and M. Scheffler, *Appl. Phys. A* **A55**, 442 (1992).
- ⁵⁴L. Q. Yang and A. E. DePristo, *J. Catal.* **149**, 223 (1994).
- ⁵⁵K. K. Nanda, A. Maisels, F. E. Kruis, H. Fissan, and S. Stappert, *Phys. Rev. Lett.* **91**, 106102 (2003).
- ⁵⁶K. Dick, T. Dhanasekaran, Z. Y. Zhang, and D. Meisel, *J. Am. Chem. Soc.* **124**, 2312 (2002).
- ⁵⁷J. P. K. Doye and F. Calvo, *J. Chem. Phys.* **116**, 8307 (2002).
- ⁵⁸S. H. Overbury, P. A. Bertrand, and G. A. Somorjai, *Chem. Rev. (Washington, D.C.)* **75**, 547 (1975).
- ⁵⁹I. Egly, G. Lohoefer, and G. Jacobs, *Phys. Rev. Lett.* **75**, 4043 (1995).
- ⁶⁰J. A. Venables, *Surf. Sci.* **299/300**, 798 (1994).
- ⁶¹J. A. Venables, *Introduction to Surface and Thin Film Processes* (Cambridge University Press, Cambridge, England, 2000).
- ⁶²J. A. Venables and J. H. Harding, *J. Cryst. Growth* **211**, 27 (2000).
- ⁶³L. J. Xu, G. Henkelman, C. T. Campbell, and H. Jonsson, *Phys. Rev. Lett.* **95**, 146103 (2005).
- ⁶⁴L. J. Xu, G. Henkelman, C. T. Campbell, and H. Jonsson, *Surf. Sci.* **600**, 1351 (2006).
- ⁶⁵A. Masson, J. J. Metois, and R. Kern, *Surf. Sci.* **27**, 463 (1971).
- ⁶⁶D. E. Starr, *Adsorption Microcalorimetry of Metal Adsorption on Single Crystal Surfaces* (Ph.D. Thesis, University of Washington, Seattle, 2001).
- ⁶⁷D. E. Starr, D. J. Bald, J. E. Musgrove, J. T. Ranney, and C. T. Campbell, *J. Chem. Phys.* **114**, 3752 (2001).
- ⁶⁸C. T. Campbell and D. E. Starr, *J. Am. Chem. Soc.* **124**, 9212 (2002).
- ⁶⁹H. Graoui, S. Giorgio, and C. R. Henry, *Philos. Mag. B* **81**, 1649 (2001).
- ⁷⁰M. Gillet, A. A. Mohammed, K. Masek, and E. Gillet, *Thin Solid Films* **374**, 134 (2000).
- ⁷¹H. Iddir, S. Ogut, N. D. Browning, and M. M. Disko, *Phys. Rev. B* **72**, 081407(2005).
- ⁷²C. R. Henry, C. Chapon, S. Giorgio, and C. Goyhenex, in *Chemisorption and Reactivity on Supported Clusters and Thin Films*, edited by R. M. Lambert and G. Pacchioni (Kluwer Acad. Publ., Amsterdam, 1997), p. 117.
- ⁷³H. J. Freund, M. Baumer, and H. Kuhlenbeck, *Adv. Catal.* **45**, 333 (2000).
- ⁷⁴D. W. Goodman, *Surf. Rev. Lett.* **2**, 9 (1995).
- ⁷⁵G. Pacchioni, N. Lopez, and F. Illas, *Faraday Discuss.* **114**, 209 (1999).
- ⁷⁶A. Howard, D. N. S. Clark, C. E. J. Mitchell, R. G. Egdell, and V. R. Dhanak, *Surf. Sci.* **518**, 210 (2002).
- ⁷⁷J. A. Rodriguez, G. Liu, T. Jirsak, J. Hrbek, Z. P. Chang, J.

- Dvorak, and A. Maiti, *J. Am. Chem. Soc.* **124**, 5242 (2002).
- ⁷⁸N. Lopez, J. K. Norskov, T. V. W. Janssens, A. Carlsson, A. Puig-Molina, B. S. Clausen, and J. D. Grunwaldt, *J. Catal.* **225**, 86 (2004).
- ⁷⁹F. Cosandey, L. Zhang, and T. E. Madey, *Surf. Sci.* **474**, 1 (2001).
- ⁸⁰C. G. Granqvist and R. A. Buhrman, *Appl. Phys. Lett.* **27**, 693 (1975).
- ⁸¹C. G. Granqvist and R. A. Buhrman, *J. Catal.* **42**, 477 (1976).
- ⁸²J. Sehested, A. Carlsson, T. V. W. Janssens, P. L. Hansen, and A. K. Datye, *J. Catal.* **197**, 200 (2001).